

Realization of a cold atom gyroscope in space

Jinting Li^{1,2}, Xi Chen^{1*}, Danfang Zhang^{1,2}, Wenzhang Wang^{1,2}, Yang Zhou^{1,2}, Meng He¹, Jie Fang¹, Lin Zhou^{1,3}, Chuan He¹, Junjie Jiang^{1,2}, Huanyao Sun¹, Qunfeng Chen¹, Lei Qin¹, Xiao Li¹, Yibo Wang¹, Xiaowei Zhang¹, Jiaqi Zhong^{1,3}, Runbing Li^{1,3,5}, Meizhen An⁴, Long Zhang⁴, Shuquan Wang⁴, Zongfeng Li⁴, Jin Wang^{1,3,5,†} and Mingsheng Zhan^{1,3,5,‡}

¹State Key Laboratory of Magnetic Resonance and Atomic and Molecular Physics, Innovation Academy for Precision Measurement Science and Technology, Chinese Academy of Sciences, Wuhan 430071, China

²School of Physical Sciences, University of Chinese Academy of Sciences, Beijing 100049, China

³Hefei National Laboratory, Hefei 230088, China

⁴Technology and Engineering Center for Space Utilization, Chinese Academy of Sciences, Beijing 100094, China

⁵Wuhan Institute of Quantum Technology, Wuhan 430206, China

Corresponding authors

*chenxi@apm.ac.cn

†wangjin@apm.ac.cn

‡mszhan@apm.ac.cn

Abstract

High precision gyroscopes in space are important for sophisticated scientific experiments and deep space navigation. Microgravity in the space provides an ideal condition for operation of a cold atom gyroscope. To demonstrate this advantage, an atom interferometer (AI) was launched and installed in the China Space Station in 2022. Here reported is a realization of the cold atom gyroscope with this AI. By applying point source interferometry, spatial fringes are obtained and acceleration and rotation are extracted. The angles of the Raman lasers are precisely calibrated to avoid measurement error, and other systematic errors are also considered for the rotation measurement. The evaluated rotation measurement is $(-115.64 \pm 1.71) \times 10^{-5}$ rad/s in space, and an acceleration measurement resolution of 1.03×10^{-6} m/s² is also obtained for a single image. This study conducts the first AI-based gyroscope in space and paves a way for future space-based AI experiments.

Keywords

Space cold atom gyroscope, Point source atom interferometry, Acceleration measurement

Introduction

Atom interferometers (AIs) are used for high-precision measurement of gravity, rotation, gravity gradient, equivalence principle (EP) test, gravitational wave detection, etc¹⁻¹². To improve the sensitivity, long-baseline AIs have been built on the ground¹³⁻¹⁷, and others have been proposed¹⁸⁻²². In space, benefitting from the microgravity environment, the interrogation time is much longer than that of the ground-based experiment, and much higher measurement precision is expected. Projects for earth gravity field measurement^{23,24}, EP tests^{25,26}, gravitational wave detection²⁷⁻²⁹, and dark matter detection^{27-28,30} are proposed. Preliminary studies have been carried out at the same time. Projects such as ICE³¹⁻³³, QUANTUS³⁴⁻³⁶, MAIUS^{37,38}, Cold Atom Laboratory

(CAL)³⁹⁻⁴², and The Cold Atom Physics Research Rack (CAPR)⁴³ are implemented.

Gyroscope has important applications in geoscience research, navigation, and fundamental physics research. Space-domain interferometer with atomic beams and time-domain with cold atoms are proposed for the rotation measurement^{6,8,10}. Methods such as four-pulse gyroscope sequence^{7,9} and point source atom interferometry are also proposed^{14,44-46}. The reported highest resolution in the earth is 3×10^{-10} rad/s up to now⁹. The gravity of the earth is the main reason that limits the interrogation time of interference and thus the resolution of the gyroscopes. The microgravity in the space provides an ideal environment for AI experiments. For example, the HYPER project is designed to realize an AI-based gyroscope with high sensitivity in space and to test the Lense-Thirring effect with a precision of 1%⁴⁷. Besides the scientific motivations, precision gyroscope in space can be also used to improve the attitude control and navigation precision for the spacecraft.

The China Space Station Atom Interferometer (CSSAI) is an integrated ^{85}Rb - ^{87}Rb dual-species atom interferometer payload. Its scientific goal is to perform in-orbit experiments for the atom interferometry measurements and equivalence principle (EP) test. The ground functional test was carried out⁴⁸, and the payload was launched into the China Space Station (CSS) by the Tianzhou-5 cargo spacecraft in November 2022. After more than one year of in-orbit experiments, the functionality of the payload is confirmed. The cooling, state preparation, and fluorescence detection processes are optimized. The Mach-Zenden (M-Z) type interferometer for the ^{85}Rb and ^{87}Rb atoms is achieved.

Here, we report the rotation measurement result by the CSSAI. By applying the point source interferometry (PSI)¹⁴ and double single diffraction (DSD) methods³³, spatial fringes are obtained and the rotation and acceleration signal are extracted. The angles of the Raman lasers are precisely calibrated in orbit to avoid rotation measurement errors. Other systematic errors are also considered and corrected. The measurement result of the rotation coincides well with the rotation measured by the CSS platform. The result provides the first AI-based Gyroscope in space and paves a way for the implementation of satellite-based cold-atom inertial sensors.

Results

The CSSAI contains three systems: the physical, optical, and electronic systems, as shown in Figure 1c. The physical system is for cooling and interference of atoms. Its core component is a vacuum chamber with a vacuum value at a level of 10^{-8} Pa. An inertial measuring unit (IMU) is installed inside the physical system to monitor acceleration and rotation. The optical system provides lasers for atom manipulation. Lasers are coupled to three single-mode polarization-maintaining (SMPM) fibers and sent to the physical system, acting as the two-dimensional magneto-optical trap (2D-MOT), three-dimensional magneto-optical trap (3D-MOT), and Raman lasers, respectively. The electronic system drives and controls the payload. Detailed introductions of the payload are introduced in ref. 48. Owing to restricted installation space and power constraints, the payload is designed with a size of 46 cm \times 33 cm \times 26 cm and a maximum power consumption of about 75 W. The payload is operated in remote mode. Operational commands are sent to the payload from the Payload Operation and Application Center (POAC) of the CSS on the ground. The experimental data are transmitted from the payload to the POAC for real-time data monitoring and post-data processing.

The CSSAI is installed inside the Free-floating Platform for Microgravity Experiment (FPME) of the High Microgravity Level Research Rack (HMLR) in the CSS, as shown in Figure 1a and 1b.

The FPME has a two-layer structure. The positions and attitudes of the two layers are controlled by gas thruster and magnetic field coils, respectively. This platform can provide a microgravity environment of 10^{-7} g level. The CSSAI is installed on the mounting board of the inner layer. So, the payload has no effective heat-dissipation channel, and the temperature continues to rise when it operates. To maintain the stability of the payload's parameters and protect the payload from overheating, the CSSAI is operated intermittently. Each experiment lasts for 50-70 min and the temperature rises for about 6 °C. In the first 10 min, the payload is turned on. The temperatures of the lasers and Rb vapor cells are controlled, and the frequencies of seed lasers are auto-locked. In the next 20 min, the preset atom interference experiment time sequence is executed periodically. In the last 20-40 min, the payload is operated in a standby mode to minimize the power consumption. Experiment data are transmitted to the host computer of the CSS. Then, the payload is powered off and naturally cooled to the room temperature of the CSS for 3-4 hours.

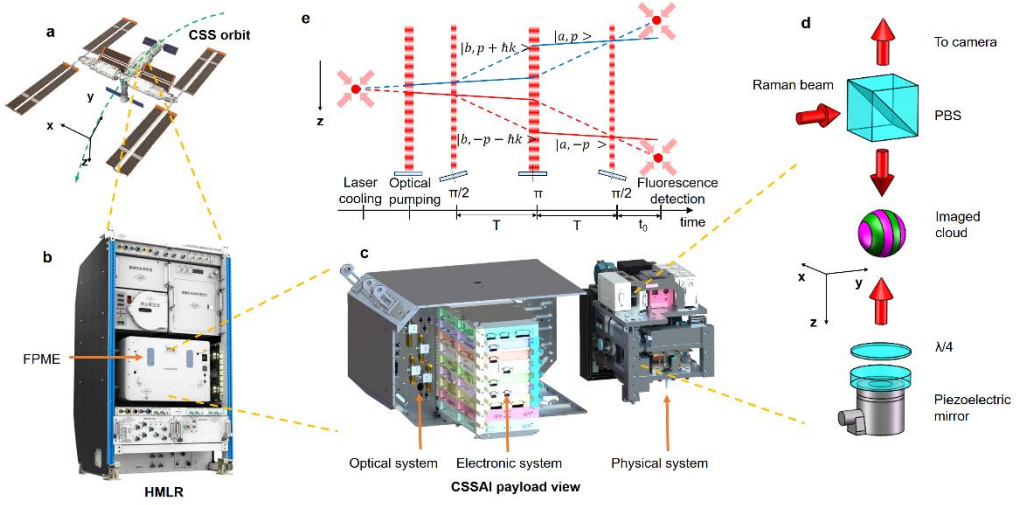


Figure 1. The China Space Station Atom Interferometer (CSSAI) configuration. **a** The China Space Station (CSS), its orbit, and the definition of the coordinate. **b** The High Microgravity Level Research Rack (HMLR) in the CSS. In the center of HMLR is the Free-floating Platform for Microgravity Experiment (FPME), and the CSSAI is installed in it. **c** The CSSAI payload and its sub-systems. **d** Scheme to realize the point source interferometry (PSI) and to collect the atom fluorescence. **e** The principle of the double single diffraction (DSD) scheme. $|a\rangle$ and $|b\rangle$ represent the $|5^2S_{1/2}, F=1, m_F=0\rangle$ and $|5^2S_{1/2}, F=2, m_F=0\rangle$ states for ^{87}Rb atom.

The principle of atom interference and fluorescence detection of CSSAI is shown in Figure 1e. ^{87}Rb atom clouds with more than 10^8 atoms and a temperature of $2 \mu\text{K}$ (see Method 1) are produced using 2D-MOT and 3D-MOT. The atoms are then optically pumped to the $|5^2S_{1/2}, F=1\rangle$ state. The DSD Raman transition scheme is applied to create two symmetrical M-Z interference loops composed of states $|5^2S_{1/2}, F=2, m_F=0\rangle$ and $|5^2S_{1/2}, F=1, m_F=0\rangle$. The duration of the π pulse is set to be $17 \mu\text{s}$ and the two-photon detuning is set to be 74 kHz . Because of the microgravity in space, there is no need to compensate for the Doppler shift of the Raman transition. The two-photon detuning is kept the same for the three Raman pulses. A closed-loop two-axis piezoelectric mirror is used to control the angle of the Raman laser. This device is used to realize the PSI. After the interference, atoms in the $|5^2S_{1/2}, F=2\rangle$ state are fluorescently excited. The fluorescence is imaged in the same direction as the Raman laser through a polarization beam splitter (PBS), and imaged by

a SCMOS camera, as shown in Figure 1d. The phase of the atom after the interference is

$$\phi = k_{eff}a_z T^2 + \sum_{i=x,y} k_{eff} [2\Omega_j v_i T^2 + \theta_{j,1} r_i + \theta_{j,3} (r_i + 2v_i T)], \quad (1)$$

where k_{eff} is the effective wave vector, T is the time interval between the Raman pulses, $i=x,y$ and $j=y,x$ is the opposite of i , a_z is the residual acceleration in the z -axes, Ω_j is the rotation of CSS in the j -axes and $\theta_{j,1}$ and $\theta_{j,3}$ are the angles of the piezoelectric mirror in the j -axes at the time of the 1st and 3rd Raman laser pulses relative to the angle at the time of the 2nd Raman laser pulse. r_i and v_i are the position and velocity of the atom at the time of the 1st Raman laser pulse. The imaging process will project the 3D population of the atom cloud to the 2D imaging plane. According to equation (1), the phase is varied in the x and y direction, and the imaging plane of the imaging system is also in the x - y plane. Due to the consistency of these directions, the formula of the phase of the 2D spatial fringe is the same as that of equation (1).

The phase is related to the position and velocity of the atom at the time of the 1st Raman laser pulse. However, for the fluorescence image, what we measured is the spatial population of the atom at the fluorescence detection time. One has $R_i = r_i + v_i(2T + t_0)$, where R_i is the position of the atom at the fluorescence detection time and t_0 is the time interval between the 3rd Raman laser pulse and fluorescence excitation laser pulse. For the general case, the position and velocity distribution of the atom will induce decoherence and period variation for the spatial fringe⁴⁴. By proper adjusting $\theta_{j,1}$ and $\theta_{j,3}$, as illustrated in ref. 17 and Method 2, the phase is only related to R_i . The phase of the spatial fringe is expressed as

$$\phi = k_{eff}a_z T^2 + \sum_{i=x,y} f_i R_i, \quad (2)$$

$$f_i = \frac{2k_{eff}}{2T+t_0} (\theta_{j,3} T + \Omega_j T^2), \quad (3)$$

where f_i is the spatial frequency of the spatial fringe. This procedure decouples the phase of the spatial fringe from the position and velocity distribution of the atom and is the basis of precision rotation measurement by using the PSI method.

Calibration of the angle of the piezoelectric mirror in space

The rotation is calculated through the measured spatial frequency f_i of the spatial fringe and the setting value of the angle of the piezoelectric mirror θ_j according to equation (3). The precision of the θ_j is essential to the precision of the rotation measurement. θ_j is proportional to its control voltage V_j with $\theta_j = \alpha_j V_j$, where α_j is the voltage-angle coefficient. In-orbit atom interference experiments are carried out to calibrate these coefficients. We change the value of V_j to modulate f_i . The value of α_j is obtained through linear fitting with a series value of f_i and V_j . The result is shown in Figure 2. The calculated coefficients are $\alpha_x = 118.99 \pm 0.50 \mu\text{rad/V}$ and $\alpha_y = 118.15 \pm 0.23 \mu\text{rad/V}$. Besides, the rotation is also obtained from the fitting result, The calculated rotation value is $\Omega_x = (-116.05 \pm 1.45) \times 10^{-5} \text{ rad/s}$, and $\Omega_y = (3.42 \pm 0.63) \times 10^{-5} \text{ rad/s}$. The CSS's orbit is in a nadir-pointing mode. Ω_x and Ω_y represent the projection of the rotation rate in the x and y direction.

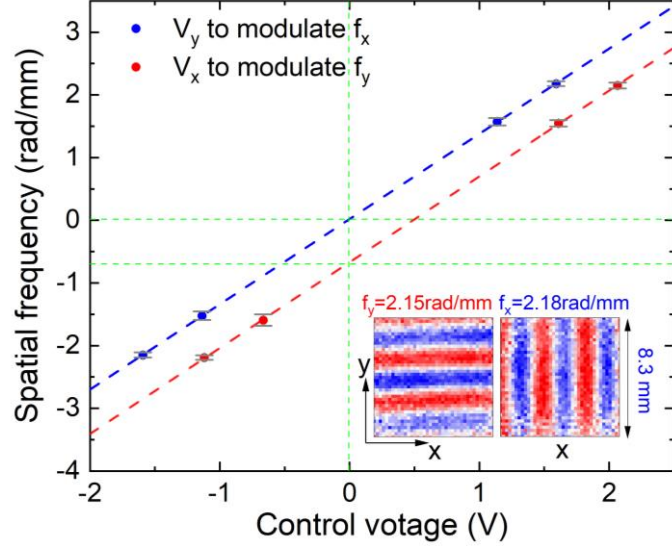


Figure 2. Calibration of the voltage-angle coefficient α_j by measuring the spatial fringe's spatial frequency f_i with $T = 50$ ms. The dots are the measured spatial frequencies relative to the control voltages. The dashed lines are line-fitting curves. The inset images are the 2nd order of principal component analysis (PCA) of the interference images.

Rotation and acceleration extraction in space

To measure Ω_x more precisely. Interference experiments with $T=75$ ms are carried out. f_y is set to approximately 1.5 rad/mm according to Ω_x and the calibrated $\theta_{x,3}$ with equation (3). The measured fluorescence image is averaged in the x-direction. This produce will transfer the spatial fringe from 2D to 1D. The spatial frequency f_x has no contribution to the spatial frequency of the averaged 1D fringe, and the spatial frequency of the 1D interference fringe is just f_y . The interference fringe is printed on the envelope of the atomic cloud. To simplify the curve fitting formula, a normalization procedure is designed to decouple the fringe from the atomic fluorescence's envelope and normalize its offset and amplitude over position (see Method 3). The population of the treated fringe is expressed as

$$P = A + C \cos[k_{eff} a_z T^2 + f_y R_y], \quad (4)$$

where A and C denote the bias and amplitude of the fringes. The values of Ω_x and a_z are obtained through cosine fitting by using equation (4). 230 sets of fringes are treated, and the fitting results are shown in Figure 3a. The Allan derivation of rotation measurement is 1.26×10^{-5} rad/s with an average point of 32, as shown in Figure 3b. For comparison, the rotation measured by the CSSAI's IMU and the CSS platform is also recorded during the same time interval. The standard deviations are 0.48×10^{-5} rad/s and 0.18×10^{-5} rad/s. The rotation measurement fluctuation of AI is much higher than that of the CSSAI's IMU and the CSS platform. So, this fluctuation is mainly caused by the measurement noise of AI but not the rotation variation of CSS itself. For the acceleration measurement, its induced phase variation exceeds 2π owing to the large vibration noise of the CSS. Therefore, an accurate acceleration value is not given, but the resolution of the acceleration is evaluated by the fitting residual, which is 1.03×10^{-6} m/s² for a single measurement.

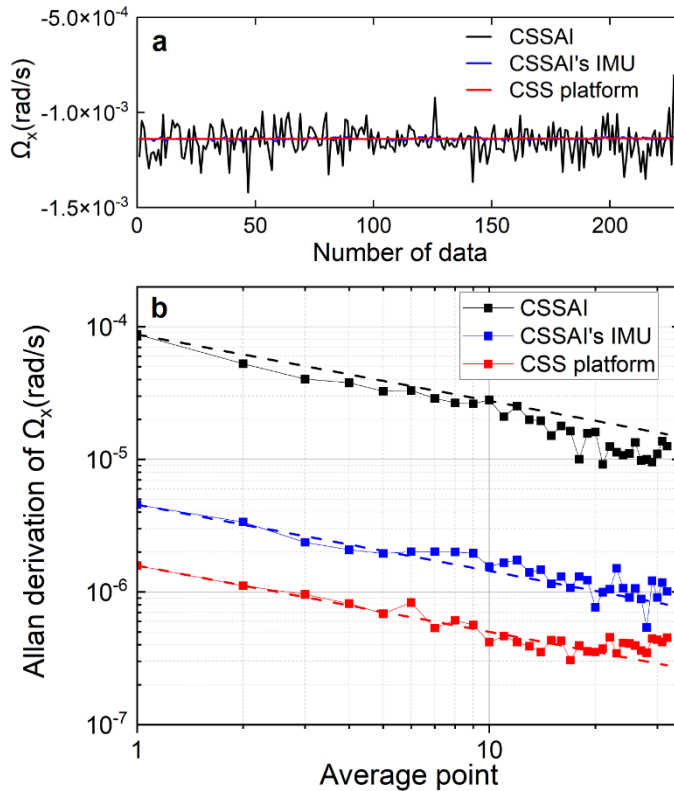


Figure 3. Rotation measurement in space. **a** Measured value for rotation Ω_x by using the CSSAI, CSSAI's IMU, and the CSS platform. **b** Allan derivation for the rotation measurement. The dots are the calculated Allan derivations, and the dashed lines are the theoretical $1/\sqrt{n}$ curves.

Systemic error estimation of the rotation measurement

Systemic error terms are evaluated to obtain the accuracy rotation value. The angle of the piezoelectric mirror is adjusted according to Method 2. However, the angle adjustment is not perfect. Its uncertainty will induce error for the period of the spatial fringe and thus the rotation measurement value. This measurement error is calculated and corrected. The fluctuations of the position and velocity of the atomic cloud are measured in Method 1. These fluctuations will couple to the residual angle error and induce fluctuation of the spatial frequency. The influence of the uncertainty of the Raman laser frequency and interrogation time is evaluated using equation (2). The finite-time effect of Raman laser pulses is also considered and corrected. The gradient of the magnetic field is estimated using the ground test results, and its influence on the spatial fringe is calculated. Other effects, such as residual acceleration, AC Stack shift, and multi-sideband effect⁴⁹, that only influence the phase but not the spatial frequency are not listed. The calculation results are presented in Table 1. The evaluated rotation value is $\Omega_x = (-115.64 \pm 1.71) \times 10^{-5}$ rad/s. For comparison, the rotation measured by the CSSAI's IMU and the CSS platform in the same time interval is also recorded. The values are $(-113.91 \pm 0.10) \times 10^{-5}$ rad/s and $(-113.87 \pm 0.05) \times 10^{-5}$ rad/s, respectively. The three measured values are in good agreement with each other.

Table 1. Precision evaluation for the rotation measurement

Error	Value (10^{-5} rad/s)	Uncertainty (10^{-5} rad/s)
Measurement result	-115.01	1.26
Angle error of the piezoelectric mirror	-0.63	1.16
Atom parameters	-	<0.01
Laser frequency	-	<0.01
Time uncertainty	-	<0.01

Magnetic field	-	0.01
Total	115.64	1.71

Discussion

This article reports the first AI-based gyroscope in space. The measurement precision is in the order of 10^{-5} rad/s. The relatively low rotation measurement precision is mainly caused by the small interference loop area. The interference loop area is proportional to vT^2 . For our experiment, the velocity is the thermal expansion velocity of the cold atom cloud, and the interrogation time is less than 100 ms. For more ambitious space AI-based gyroscope, such as the HYPER project⁴⁷, a higher velocity of the atom cloud and longer interrogation time of the interference is needed.

The PSI method can eliminate the decoherent effect of the atom cloud and enhance the contrast of the interference fringe. However, the induced rotation of the Raman laser might cause additional measurement uncertainty. For example, the uncertainty of the rotation axis and rotation angle will cause measurement uncertainty both for the rotation and acceleration measurements. So, the PSI method might not be the best choice for high-precision space AI-based experiments. For example, the GRICE project proposes to use the ultracold atom cloud to enhance the interference fringe's contrast, rather than compensate for the rotation⁵⁰.

Two reasons that limit the interference time of our experiment. One is the low signal-to-noise ratio, which is caused by low participated interference atom number and large detection noise caused by the stray light. This could be improved by lowering the temperature and enhancing the number of atom clouds and avoiding stray light in the next version of the payload design. The other is the low contrast of the interference fringe, which is only 2% for our experiment. This might be caused by the imperfect Raman laser's polarization or the large phase noise of the microwave for the Raman laser, which is still under investigation.

The EP test is one of the most important scientific objectives of CSSAI. For an EP test experiment, what we measured is the differential acceleration. Most measurement errors are in common for the synchronously measured dual-species AI. For example, the residual acceleration of the CSS platform, and the error caused by the angle and axis uncertainty of the piezoelectric mirror are in common. Therefore, the EP test precision will be much higher than that of the acceleration measurement. The compact design, the in-orbit calibration of the PSI parameters, and the scheme of rotation and acceleration extraction in space provide a foundation for future space experiments based on AIs.

Methods

1. Parameters measurement of the cold atom cloud

The temperature of the cold-atom cloud is essential for extending the interrogation time. The position and velocity of the cold atom cloud are important parameters for estimating the systemic error of both acceleration and rotation measurements. Therefore, for the AI-based rotation measurement in this article, the cold atom cloud at the end of the MOT stage and at the time of the fluorescence detection stage are imaged. The position, velocity, and temperature of the cold atom cloud are measured by using the time-of-flight (TOF) method. The measurement results are shown in Figure 4. The position variations of the cold atom cloud in the x and y directions are $27 \mu\text{m}$ and $19 \mu\text{m}$. The velocities of the cold atom cloud in the x and y directions are $51 \pm 89 \mu\text{m/s}$ and $2730 \pm 146 \mu\text{m/s}$. The temperatures of the cold atom cloud in the x and y directions are $2.94 \pm 0.06 \mu\text{K}$ and $2.02 \pm 0.05 \mu\text{K}$.

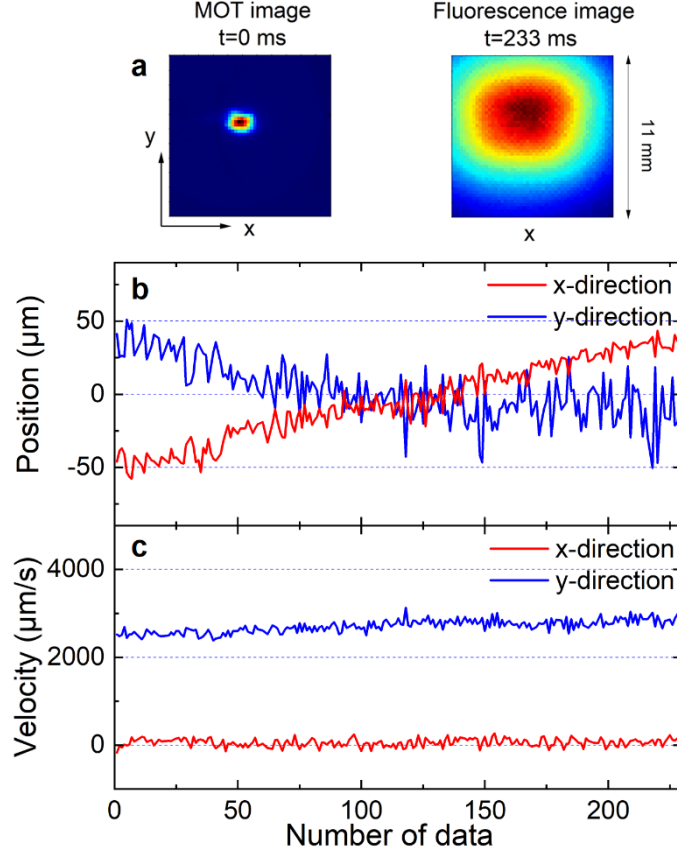


Figure 4. Parameters measurement of the cold atom cloud. **a** Atom fluorescence image at the MOT stage and the fluorescence detection stage. **b** Position variation of the atom cloud at the MOT stage. **c** Measured velocity of the atom cloud by using the time-of-flight (TOF) method.

2. Optimization of the piezoelectric mirror's angles

The interference phase is expressed as equation (1). What we measured is the atom population relative to the atom position R_i at the time of fluorescence detection. One has $R_i = r_i + v_i(2T + t_0)$. In equation (1), ϕ is related to both the position and velocity of the atom. Therefore, the fluctuations and distributions of the position and velocity of the atom induce phase measurement uncertainty and fringe decoherence. To overcome this problem, we substitute $r_i = R_i - v_i(2T + t_0)$ into equation (1), and let the coefficient of v_i to be zero. This will lead the following relationship

$$\theta_{j,1} = \frac{-t_0\theta_{j,3} + 2\Omega_j T^2}{2T + t_0}. \quad (4)$$

So, by properly adjusting the angle of the piezoelectric mirror, ϕ_i is only relate to R_i , both the effects of the offset and distributions of the position and velocity of the atom are eliminated, and the contrast of the fringe will be maximized. By substituting equation (4) into equation (1), we obtain equation (2).

3. Normalization treatment of spatial interference fringes

The 1D spatial fringe overlaps with the background of the atomic cloud fluorescence. A typical curve is shown in Figure 5a. Because of the irregular shape and position fluctuation of the cold atom cloud. It is difficult to determine a suitable formula for fitting the curve directly. Therefore, a procedure is designed to normalize the curve to a sine curve before the fitting process. First, the original curves are divided by their Gaussian fitting curves to eliminate the envelopes. The processed curves after this stage are shown in Figure 5b. The fluctuation of the curves indicates the

offset variation along the y-direction, and their average is also calculated and shown. Second, All the treated curves in Figure 5b are divided by their averaged and are then subtracted by 1. The processed curves after this stage are shown in Figure 5c. The fluctuation of the curves indicates the amplitude variation along the y-direction, and their standard derivation is also calculated and shown. Finally, the treated curves in Figure 5c are divided by their standard derivation. A typically treated fringe curve is shown in Figure 5d. Cosine fitting is used to extract the spatial frequencies and phases of the fringes.

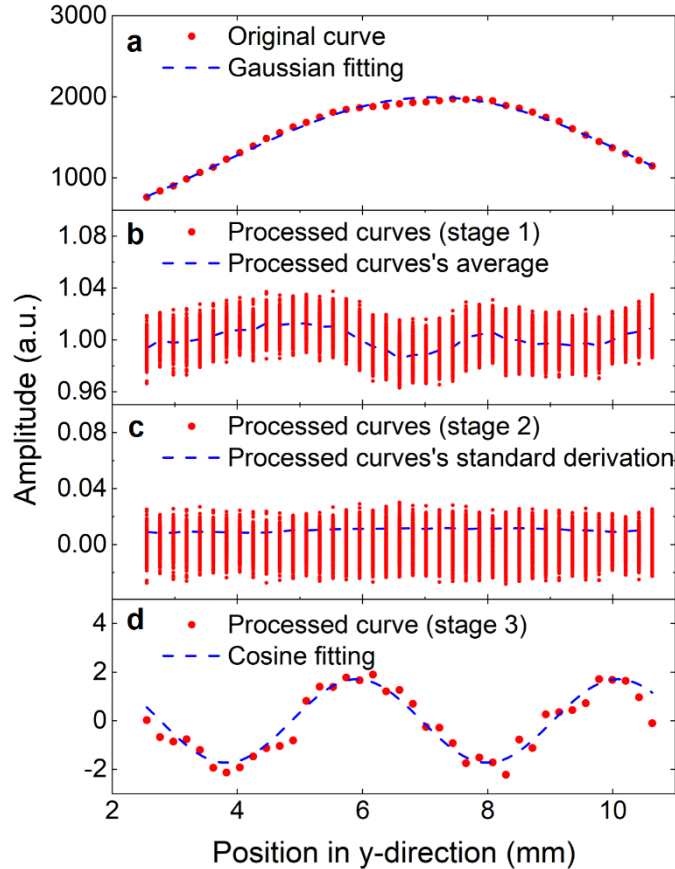


Figure 5. Normalization treatment procedure of the spatial interference fringes. **a** A typical original 1D spatial interference fringe in the y-direction. The dots are the measured curve and the dashed line is its Gaussian fitting. **b** 230 sets of treated fringes after eliminating the Gaussian envelopes. The dots are the treated curves and the dashed line is their average. **c** 230 sets of treated fringes after normalizing their offset. The dots are the treated curves and the dashed line is their standard derivation. **d** A typical treated fringe after normalizing its amplitude. The dots are the treated curve and the dashed line is its cosine fitting.

Data availability

The data that support the findings of this study are available from the corresponding author upon reasonable request.

Code availability

The codes that support the findings of this study are available from the corresponding author upon reasonable request.

Acknowledgments

We would like to thank the support from the Technology and Engineering Center for Space

Utilization, especially Hongen Zhong, Xuzhi Li, Shan Jin, and many others for their constructive discussions and technical support. This work was supported by the Second Batch of Scientific Experiment Project of the Space Engineering Application System of the China Space Station. We acknowledge support from the Innovation Program for Quantum Science and Technology (2021ZD0300603, 2021ZD0300604), the Hubei Provincial Science and Technology Major Project (ZDZX2022000001), the China Postdoctoral Science Foundation (2020M672453), National Natural Science Foundation of China (12204493), and the Wuhan Dawn Plan Project (2023010201020282).

Author contributions

X. C. designed and charged the experiment. J. T. L., D. F. Z., and M. H. analyzed and processed the data. J. T. L., D. F. Z., W. Z. W., and Y. Z. operated the in-orbit experimental and collected the data. J. T. L. and J. F. conducted the ground comparison experiment. J. T. L., L. Z., C. H., and J. J. J. analyzed the precision of the rotation measurement. H. Y. S., Q. F. C., L. Q., X. L., Y. B. W., X. W. Z., R. B. L., and J. Q. Z. supported the in-orbit experiment in the optical system analysis, the electronic system analysis, and the software operation. M. Z. A., L. Z., S. Q. W., and Z. F. L. provided the required conditions of FPME for the in-orbit experiment. X. C. and J. T. L. prepared the manuscript. M. S. Z. and J. W. coordinated with the principal members as the project scientists. All authors have read and approved the final manuscript.

Competing Interests

The authors declare no competing interests.

References

- [1] Peters, A., Chung, K. Y. & Chu, S. Measurement of gravitational acceleration by dropping atoms. *Nature* **400**, 849-852 (1999).
- [2] Merlet, S., *et al.* Comparison between two mobile absolute gravimeters: optical versus atomic interferometers. *Metrologia* **47**, L9 (2010).
- [3] Zhou, L., *et al.* Measurement of Local Gravity via a Cold Atom Interferometer. *Chin. Phys. Lett.* **28**, 013701 (2011).
- [4] Hu, Z. K., *et al.* Demonstration of an ultrahigh-sensitivity atom-interferometry absolute gravimeter. *Phys. Rev. A* **88**, 043610 (2013).
- [5] Hauth, M., Freier, C., Schkolnik, V., Senger, A., Schmidt, M. & Peters, A. First gravity measurements using the mobile atom interferometer GAIN. *Appl. Phys. B* **113**, 49-55 (2013).
- [6] Gustavson, T. L., Bouyer, P. & Kasevich, M. A. Precision rotation measurements with an atom interferometer gyroscope. *Phys. Rev. Lett.* **78**, 2046-2049 (1997).
- [7] Stockton, J. K., Takase, K. & Kasevich, M. A. Absolute Geodetic Rotation Measurement Using Atom Interferometry. *Phys. Rev. Lett.* **107**, 133001 (2011).
- [8] Xue, H. B., *et al.* A continuous cold atomic beam interferometer. *J. Appl. Phys.* **117**, 094901 (2015).
- [9] Savoie, D., Altorio, M., Fang, B., Sidorenkov, L. A., Geiger, R. & Landragin, A. Interleaved atom interferometry for high-sensitivity inertial measurements. *Sci. Adv.* **4**, eaau7948 (2018).
- [10] Yao, Z. W., *et al.* Self-alignment of a large-area dual-atom-interferometer gyroscope using parameter-decoupled phase-seeking calibrations. *Phys. Rev. A* **103**, 023319 (2021).
- [11] Cronin, A. D., Schmiedmayer, J. & Pritchard, D. E. Optics and interferometry with atoms and molecules. *Rev. Mod. Phys.* **81**, 1051-1129 (2009).
- [12] Wang, J., Zhou, L., Li, R. B., Liu, M. & Zhan, M. S. Cold atom interferometers and their

applications in precision measurements. *Front. Phys. China* **4**, 179-189 (2009).

[13] Zhou, L., *et al.* Development of an atom gravimeter and status of the 10-meter atom interferometer for precision gravity measurement. *Gen. Relativ. Gravit.* **43**, 1931-1942 (2011).

[14] Dickerson, S. M., Hogan, J. M., Sugarbaker, A., Johnson, D. M. S. & Kasevich, M. A. Multiaxis Inertial Sensing with Long-Time Point Source Atom Interferometry. *Phys. Rev. Lett.* **111**, 083001 (2013).

[15] Hartwig, J., *et al.* Testing the universality of free fall with rubidium and ytterbium in a very large baseline atom interferometer. *New J. Phys.* **17**, 035011 (2015).

[16] Zhou, L., *et al.* Test of Equivalence Principle at 10^{-8} Level by a Dual-Species Double-Diffraction Raman Atom Interferometer. *Phys. Rev. Lett.* **115**, 013004 (2015).

[17] Asenbaum, P., Overstreet, C., Kim, M., Curti, J. & Kasevich, M. A. Atom-Interferometric Test of the Equivalence Principle at the 10^{-12} Level. *Phys. Rev. Lett.* **125**, 5 (2020).

[18] Canuel, B., *et al.* Exploring gravity with the MIGA large scale atom interferometer. *Sci. Rep.* **8**, 14064 (2018).

[19] Zhan, M. S., *et al.* ZAIGA: Zhaoshan long-baseline atom interferometer gravitation antenna. *Int. J. Mod. Phys. D* **29**, 1940005 (2020).

[20] Badurina, L., *et al.* AION: an atom interferometer observatory and network. *J. Cosmol. Astropart. Phys.* **2020**, 011 (2020).

[21] Canuel, B., *et al.* ELGAR-a European Laboratory for Gravitation and Atom-interferometric Research. *Class. Quantum Gravity* **37**, 225017 (2020).

[22] Abe, M., *et al.* Matter-wave Atomic Gradiometer Interferometric Sensor (MAGIS-100). *Quantum Sci. Technol.* **6**, 044003 (2021).

[23] Trimeche, A., *et al.* Concept study and preliminary design of a cold atom interferometer for space gravity gradiometry. *Class. Quantum Gravity* **36**, 215004 (2019).

[24] Lévèque, T., *et al.* Gravity field mapping using laser-coupled quantum accelerometers in space. *J. Geodesy* **95**, 15 (2021).

[25] Altschul, B., *et al.* Quantum tests of the Einstein Equivalence Principle with the STE-QUEST space mission. *Adv. Space Res.* **55**, 501-524 (2015).

[26] Amelino-Camelia, G., *et al.* GAUGE: the GrAnd Unification and Gravity Explorer. *Exp. Astron.* **23**, 549-572 (2009).

[27] Bertoldi, A., *et al.* AEDGE: Atomic experiment for dark matter and gravity exploration in space. *Exp. Astron.* **51**, 1417-1426 (2021).

[28] Tino, G. M., *et al.* SAGE: A proposal for a space atomic gravity explorer. *Eur. Phys. J. D* **73**, 228 (2019).

[29] Wang, G., Gao, D., Ni, W.-T., Wang, J. & Zhan, M. Orbit design for space atom-interferometer AIGSO. *Int. J. Mod. Phys. D* **29**, 1940004 (2020).

[30] Wolf, P., *et al.* Quantum physics exploring gravity in the outer solar system: the SAGAS project. *Exp. Astron.* **23**, 651-687 (2009).

[31] Stern, G., *et al.* Light-pulse atom interferometry in microgravity. *Eur. Phys. J. D* **53**, 353-357 (2009).

[32] Geiger, R., *et al.* Detecting inertial effects with airborne matter-wave interferometry. *Nat. Commun.* **2**, 474 (2011).

[33] Barrett, B., *et al.* Dual matter-wave inertial sensors in weightlessness. *Nat. Commun.* **7**, 13786 (2016).

[34] van Zoest, T., *et al.* Bose-Einstein Condensation in Microgravity. *Science* **328**, 1540-1543 (2010).

[35] Rudolph, J., *et al.* Degenerate Quantum Gases in Microgravity. *Microgravity Sci. Technol.* **23**, 287-292 (2011).

[36] Müntinga, H., *et al.* Interferometry with Bose-Einstein Condensates in Microgravity. *Phys. Rev. Lett.* **110**, 093602 (2013).

[37] Becker, D., *et al.* Space-borne Bose-Einstein condensation for precision interferometry. *Nature* **562**, 391- 395 (2018).

[38] Lachmann, M. D., *et al.* Ultracold atom interferometry in space. *Nat. Commun.* **12**, 1317 (2021).

[39] Frye, K., *et al.* The Bose-Einstein Condensate and Cold Atom Laboratory. *EPJ Quantum Technol.* **8**, 1 (2021).

[40] Aveline, D. C., *et al.* Observation of Bose-Einstein condensates in an Earth-orbiting research lab. *Nature* **582**, 193-197 (2020).

[41] Carollo, R. A., *et al.* Observation of ultracold atomic bubbles in orbital microgravity. *Nature* **606**, 281-286 (2022).

[42] Elliott, E. R., *et al.* Quantum gas mixtures and dual-species atom interferometry in space. *Nature* **623**, 502-508 (2023)

[43] Li, L., *et al.* The Design, Realization, and Validation of the Scheme for Quantum Degenerate Research in Microgravity. *IEEE Photonics J.* **15**, 1-8 (2023).

[44] Sugarbaker, A., Dickerson, S. M., Hogan, J. M., Johnson, D. M. S. & Kasevich, M. A. Enhanced Atom Interferometer Readout through the Application of Phase Shear. *Phys. Rev. Lett.* **111**, 113002 (2013).

[45] Hoth, G. W., Pelle, B., Riedl, S., Kitching, J. & Donley, E. A. Point source atom interferometry with a cloud of finite size. *Appl. Phys. Lett.* **109**, 071113 (2016).

[46] Chen, Y. J., Hansen, A., Hoth, G. W., Ivanov, E., Pelle, B., Kitching, J. & Donley, E. A. Single-Source Multiaxis Cold-Atom Interferometer in a Centimeter-Scale Cell. *Appl. Phys. Lett.* **12**, 014019 (2019).

[47] Jentsch, C., Müller, T., Rasel, E. M. & Ertmer, W. HYPER: A Satellite Mission in Fundamental Physics Based on High Precision Atom Interferometry. *Gen. Relativ. Gravit.* **36**, 2197-2221 (2004)

[48] He, M., *et al.* The space cold atom interferometer for testing the equivalence principle in the China Space Station. *NPJ Microgravity* **9**, 58 (2023).

[49] Carraz, O., Charrière, R., Cadoret, M., Zahzam, N., Bidel, Y. & Bresson, A. Phase shift in an atom interferometer induced by the additional laser lines of a Raman laser generated by modulation. *Phys. Rev. A* **86**, 033605 (2012).

[50] Lévèque, T., et al Gravity field mapping using laser-coupled quantum accelerometers in Space *J. Geodesy* **95**, 15 (2021)